IEEE Access
Multidisciplinary | Rapid Review | Open Access Journal

Received September 23, 2019, accepted October 5, 2019, date of publication November 4, 2019,
date of current version November 20, 2019.

Digital Object Identifier 10.1109/ACCESS.2019.2951152

Ray Theory-Based Transcranial Phase Correction for Intracranial Imaging: A Phantom Study

CHEN JIANG[1], YUNQING LI[1], BOYI LI[1], CHENGCHENG LIU[2], FENG XU[1,3], KAILIANG XU[1,3], (Member, IEEE), AND DEAN TA[1,3]

[1]Department of Electronic Engineering, Fudan University, Shanghai 200433, China
[2]Institute of Acoustics, Tongji University, Shanghai 200092, China
[3]Zhuhai Fudan Innovation Institute, Zhuhai 519000, China

Corresponding authors: Chengcheng Liu (chengchengliu@tongji.edu.cn) and Dean Ta (tda@fudan.edu.cn)

This work was supported in part by the National Natural Science Foundation under Grant 11525416, Grant 11827808, Grant 11604054, and Grant 11804056, in part by the Natural Science Foundation of Shanghai under Grant 19ZR1402700, in part by the Shanghai Municipal Science and Technology Major Project under Grant 2017SHZDZX01, in part by the China Postdoctoral Science Foundation under Grant 2018M641924 and Grant 2019T120293, in part by the Shanghai Talent Development Fund under Grant 2018112, and in part by the State Key Laboratory of ASIC and System Project under Grant 2018MS004.

ABSTRACT Ultrasonic imaging provides a non-invasive way to diagnose brain disease. However, due to imaging degradation effects from the phase-aberration and reverberation, it is still challenging to achieve an accurate transcranial imaging. The objective of this work is to improve the quality of transcranial imaging. To this end, a ray theory based transcranial phase correction method was proposed to correct the phase abberation induced by cranial bones. With the pre-knowledge of the shape and longitudinal velocity of the cranial bones, the corrected phases are derived by solving eikonal equation (ray-theory). The Ideal Synthetic Aperture Focusing Technique (I-SAFT) is applied for signal acquisitions in simulations and in-vitro phantom experiment with one-element transmitting and all-element receiving method. Dynamic focusing is achieved at each imaging position with I-SAFT and the transcranial imaging distortion is modified with the proposed phase correction method. Simulations and experiments show that the imaging distortion of target circular phantoms was corrected, and the imaging quality is improved after the phase correction. With the proposed method, the average error of the central position of target phantoms decreases from 1.98 mm to 0.21 mm, the eccentricity of fitted ellipse averagely decreases from 0.63 to 0.19, and the average maximum luminance contrast of phantoms improves from 37.36dB to 42.41dB. It is illustrated that the proposed ray-theory based phase correction method might be useful for intracranial imaging.

INDEX TERMS Intracranial imaging, phase correction, eikonal equation, ideal synthetic aperture focusing.

I. INTRODUCTION

Ultrasound imaging, X-ray computed tomography (CT) and magnetic resonance imaging (MRI) are traditional non-invasive transcranial imaging modalities. The last two techniques have shown significant applicability to obtain high-quality images. X-ray CT, however, is unsafe for people who require continuous observation of brain diseases [1]. MRI testing is expensive, which limits its application [2]. In contrast, ultrasound has been a safe, inexpensive, and portable method to diagnose brain diseases. Transcranial ultrasound imaging (or transcranial sonography (TCS)) is a neuroimaging method that displays the brain through the skull. Its imaging principle depends on the reflection of ultrasound waves at tissue interfaces with diverse acoustic impedances to deliver information on the properties of tissues such as the basal ganglia, cerebellum, subcortical brain and midbrain structures. Transcranial ultrasound imaging is a routine technique for new-borns when the fontanelles are open [3]. For example, it is clinically applicable in new-borns in diagnosing neonatal hypoxic-ischaemic encephalopathy (HIE), neural tube defects (NTDs), etc. Transcranial ultrasound imaging has also been used to diagnose cerebral information and diseases for adults when the fontanelles are closed, *e.g.*, cerebral colour blood flow measurement with Doppler technology [4] and brainstem and subcortical brain structure assessment with B-mode sonography [5]. For instance, this imaging detects marked hyperechogenic

The associate editor coordinating the review of this manuscript and approving it for publication was Yongtao Hao.

substantia nigra (SN) in people with idiopathic Parkinson's disease [1], detects brain stem raphe hypoechogenicity in people with small vessel disease [2], and detects enlargement of the third and lateral ventricles in people with cognitive impairment [2], [3]. In addition, transcranial ultrasound imaging is a promising tool for brain tumour visualization and resection [4]. However, significant acoustic property differences between cranial bones and soft tissue invalidate the applicable prerequisite of the traditional beamforming imaging technique. Acoustic property differences, especially velocity difference, tend to cause phase deviation. Without phase correction, the phase deviation results in transcranial ultrasound defocusing, which further degrades the image quality of intracranial tissues and blood vessels [6]–[8].

Many phase correction techniques have been developed for transcranial ultrasound [10]–[20], [22], [23]. The phase correction can be accomplished by using the experimental reference signals or CT and MRI images. One of the most representative methods is the time-reversal method, where according to the acoustic reciprocity theorem [9], the temporally reversed signal can be re-emitted to achieve transcranial focusing.

The experimental signal guided techniques include the representative time-reversal method. With this method, Fink *et al*. [10] realized phase correction by assigning a single-element probe inside the cranial bones to transmit the beacon pulse signal, and a phased array probe was located outside the cranial bones as receivers. Tanter *et al*. [11] and Aubry *et al*. [12] improved the method to achieve higher-quality focusing by positioning a phased array inside the cranial bones. A spatial-temporal inverse filter matrix was established between the dual-array probes to estimate the phase correction. Those methods, however, are unrealistic in practice, as they require the presence of transducers inside the cranial bones [13]. Vignon *et al*. [14] then made further improvements by placing a pair of phase arrays on each side of the head and fabricating a virtual array between them. They established a triple layer spatial-temporal inverse filter matrix to estimate the phase correction. Another experimental signal guided technique concentrates on adaptively adjusting phases between probe elements [15], [16]. Lindsy and Smith [17] estimated the phase aberration with a multi-lag least squares estimation technique, performed by computing the normalized cross correlation between all element signals within a specified spatial lag. In addition, Clement *et al*. [18] induced shear-mode conversions at the soft tissue–skull interfaces, and phase aberrations were deduced based on the fact that the shear velocity in cranial bones is close to the longitudinal velocity in soft tissue.

Recently, CT- and MRI-guided phase correction techniques, which are based on the structural information of cranial bones, have demonstrated success for transcranial ultrasound focusing (TUS) [19], [20], [22], [23]. The techniques assume that the acoustic parameters of cranial bones vary with their spatial location [19]. The techniques include full wave simulation, using a simulated signal instead of the measured signal for time-reversal phase correction. For example, Almquist *et al*. [19] presented the hybrid angular spectrum method to simulate the received signal at the array probe. Phase aberrations were successfully corrected at multiple focusing locations based on the received signal. Marquet *et al*. [20] predicted and corrected the defocusing effect of the skull using a full 3D finite-difference simulation code together with stereotactic CT images. The full wave simulation method is computationally costly [21]. Therefore, another CT- or MRI-guided method, the ray-tracing method, was also introduced to correct phase aberrations [22], [23]. This efficient method realizes phase correction via estimating the arrival time of the wavefront [24]. For example, Jin *et al*. [22] established a triple-layer model and idealized the skull layer as homogenous. Corrected phases and amplitudes were then estimated by integrating Snell's law and the transmission coefficient of the velocity intensity and used for microwave-induced thermoacoustic tomography. Jones *et al*. [23] presented an improved multi-layered model based on the spatially independent properties of cranial bones from CT images. The phases were then corrected by calculating the refractions at each layer interface. These traditional ray tracing methods remain to be improved since it is difficult to calculate refractions through rough surfaces [25].

The present phase correction techniques require further investigation for high-quality transcranial ultrasound imaging. The paper aims to introduce a robust ray-theory-based transcranial phase correction method to improve the transcranial imaging quality. The method is inspired by seismic tomography technology, which uses backscattering waves under continuous medium interfaces to explore underground structures [24]. The method is expected to obtain the corrected phases with acoustic parameters (the shape and longitudinal velocity) of cranial bones. The corrected phases, combined with ideal synthetic aperture focusing technology (I-SAFT) and the time domain beamforming reconstruction (delay and sum, DAS) method, can achieve high-quality transcranial imaging. The paper is organized as follows: in Sec. II, the methods, including I-SAFT and ray-theory-based phase correction, are introduced. In Sec. III, the phantoms are briefly introduced, and the simulation and experimental settings on the phantoms are presented in detail. In Sec. IV, The corresponding image quality enhancement results after phase correction are quantitatively evaluated. Finally, the discussion and conclusion are presented in Sec. V and VI, respectively.

II. THEORY

A. IDEAL SYNTHETIC APERTURE FOCUSING TECHNOLOGY

The I-SAFT, originating from synthetic aperture radar technology, is generally used to improve the lateral resolution [26]. The time domain B-mode beamforming for the I-SAFT is based on a delay-and-sum (DAS) algorithm. The mathematical expression is shown as follows:

$$\bar{y}(x,z) = \frac{\sum_{i=1}^{m(x,z)} \sum_{j=1}^{m(x,z)} R_{ij}(t)_{|t=\Delta_i(x,z)+\Delta_j(x,z)}}{m(x,z)^2} \quad (1)$$

where x and z represent the spatial position of certain target points in the horizontal and vertical directions relative to the linear array, respectively; $\bar{y}(x, z)$ denotes the synthesized signal related to the target point; i is the number of active elements emitting ultrasound; j is the number of active elements receiving the signal; $m(x, z)$ represents the dynamic aperture that determines the quantity of active elements with the threshold $arctan\left[y/(m(x, z)l)\right] > \pi/4$, where l is the element spacing of the array; $R_{ij}(t)$ is the Hilbert-transformed signal received by the j-th element after the emission of the i-th element; t is the discrete time series; and $\Delta_i(x, z)$ and $\Delta_j(x, z)$ denote the discrete time series from the target point to the i-th and j-th elements, respectively. To further improve the imaging quality, noise is suppressed by adding a filtering process. The filtering process is adapted from Wiener filtering in the frequency domain [27]. The mathematical expression is as follows:

$$y_{winner} = \bar{y}\left(\bar{y}\bar{y}^*/\left(\bar{y}\bar{y}^* + (\bar{y'} - \bar{y}\bar{y}^*)/m\right)\right), \tag{2}$$

where $\bar{y'} = \sum_{i=1}^{m}\sum_{j=1}^{m} R_{ij}(t)R_{ij}(t)^*_{|t=\Delta_i+\Delta_j}/m^2$ and the symbol $*$ denotes the complex conjugate transpose operator. The spatial position (x, z) in (2) is omitted for simplicity.

The I-SAFT, symbolized with one-element transmission and all-element receiving, can achieve synthesized steering and focusing for both transmission and receiving processes. I-SAFT is suitable for transcranial phase correction imaging because the phase aberration-induced physical steering and focusing deflections for the transmission process are difficult to correct with some well-known imaging technologies,*e.g.*,plane wave [28], diverging wave [29] and focusing wave [30]. As shown in Fig. 1, the space between the linear array and craniums, as well as the space below the craniums, is assumed to be fully occupied by soft tissue. Ultrasound undergoes significant refraction (solid lines) at the cranium-tissue interfaces since the velocity difference is large between the two materials. The refractions and the velocity difference lead to time-of-flight (TOF) misestimation, which in turn results in transcranial defocusing. The TOFs Δt_i and Δt_j calculated using the ideal wavepath (dash-dotted line) are the same as the TOFs calculated using the refracted wavepath (solid line), as shown in Fig. 1. The corresponding ideal focus A is different from the real focus B in spatial positioning. The defocusing indicates that the target point B is incorrectly located at position A. The ideal wavepath originates from the assumption of conventional beamforming that ultrasound expands spherically and propagates in a line in soft tissues. The TOFs from the target point to each element of the array can be utilized for beamforming with I-SAFT for both transmission and receiving processes, as shown in (1). Improved images can be derived with the corrected TOFs.

B. THE SOLUTION OF EIKONAL EQUATIONS

The wave equation is a second-order linear partial differential equation (PDE) in homogenous media that describes ultrasonic waves as [31]:

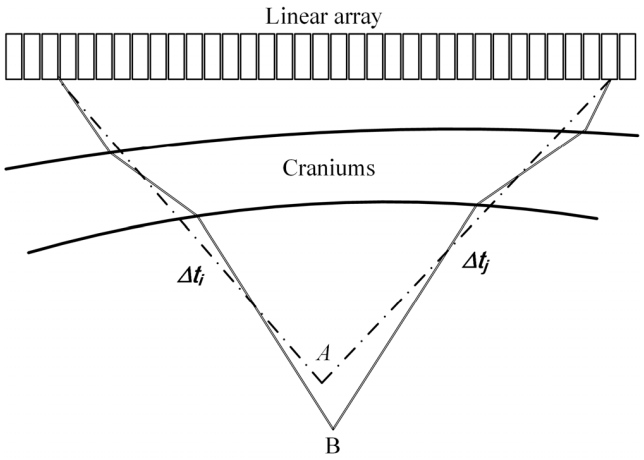

FIGURE 1. A schematic of the ideal focus (A) and real focus (B) locations. The defocusing effect is expected to induce image distortion.

$$(\nabla^2 - 1/c^2\frac{\partial^2}{\partial t^2})p = 0, \tag{3}$$

where ∇^2 is the spatial Laplacian operator, p is the sound pressure, c is the spatial varying velocity, and t represents the time. We can assume that the solution of (3) corresponding to the sinusoidal plane travelling wave has a form as follows [32]:

$$p = A(x, z)e^{-j[\omega t - k_0\varphi(x,z)]}, \tag{4}$$

where $A(x, z)$ denotes the acoustic pressure intensity; $(\omega t - k_0\varphi)$ is the wave phase; $k_0 = \omega/c_0$ denotes the reference wavenumber, where c_0 is the corresponding reference velocity; and φ denotes a spatial position relevant parameter, By substituting (4) into (3), the PDE can be simplified to two parts [32]:

$$\nabla^2\varphi + 2/(A\nabla A\nabla\varphi) = 0 \tag{5a}$$

$$(\nabla\varphi)^2 = n^2, \tag{5b}$$

where ∇ is the Del operator and $n = c_0/c$ denotes the refractivity. The spatial positions (x, z) in (5a) and (5b) are omitted for simplicity. It should be noted that the simplification is based on high-frequency approximation. Equation (5a) denotes the intensity equation that determines the ultrasound pressure amplitude. Equation (5b) denotes the eikonal equation that determines the phase of the ultrasound, which is also a form of ray acoustics. By assigning the phase of the travelling wave, the ultrasound wavefront can be obtained:

$$(\omega t - k_0\varphi(x, z)) = 0. \tag{6}$$

After integrating (5b) and (6), the eikonal equation has the following form [32]:

$$(\nabla T(x, z))^2 = 1/c(x, z)^2, \tag{7}$$

where $T(x, y)$ denotes the travel time (phases) of the ultrasound wavefront.

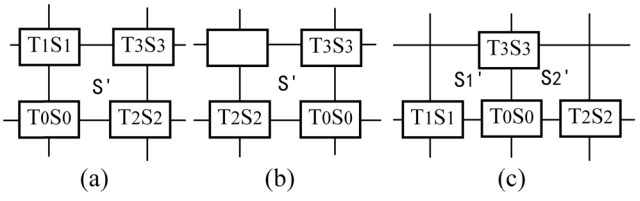

FIGURE 2. The differential grid for first arrival time calculation. (a) Calculation of T_3 with known T_0, T_1 and T_2 at the diagonal points; (b) calculation of T_3 with known T_0 and T_2, if T_1 is invalid; (c) calculation of T_3 with known T_0, T_1 and T_2 on a line.

The equation can be numerically solved with a finite difference algorithm by discretizing square grids throughout the space. We select one widely used finite difference method, namely, wavefront extrapolation [33]. The method is a repetitive process of searching the minimum time grid from the known time grids and calculating the times of the surrounding grids. The repetitive process continues until all the times in computational domain have been calculated. Fig. 2 shows the discrete form to calculate the times of the surrounding grids. The corresponding equations for the three cases are as follows [33]:

$$T_3 = T_0 + \sqrt{2\left(hS'\right)^2 - \left(T_2 - T_1\right)^2}, \tag{8a}$$

$$T_3 = T_0 + \sqrt{\left(hS'\right)^2 - \left(T_2 - T_0\right)^2}, \tag{8b}$$

$$T_3 = T_0 + \sqrt{\left(h\left(S_1' + S_2'\right)/2\right)^2 - 0.25\left(T_2 - T_1\right)^2}, \tag{8c}$$

where h is the width of the square grid; T_0 is the minimum time from the known time grids; T_2 or T_1 is the known time adjacent to T_0; and $S(x, z) = 1/c(x, z)$ denotes the spatial slowness, where S_0, S_1, S_2 and S_3 are the corresponding discrete forms to $S(x, z)$.

Fig. 2(a) shows the calculation of T_3 based on (8a), where the times T_0, T_1 and T_2 at three corners of the square cell were calculated. The centre slowness changes to $S' = \left(S_1 + S_2 + S_3 + S_0\right)/4$. Fig. 2(b) shows the calculation of T_3 based on (8b), where the times T_0 and T_2 at two corners of the square cell have been calculated. The centre slowness S' changes to $\left(S_2 + S_3 + S_0\right)/3$. Fig. 2(c) shows the calculation of T_3 based on (8c), where the times T_0, T_1 and T_2 of three consecutive points on a line have been calculated. The centre slowness S_1' and S_2' are consistent with that shown in Fig. 2(a). With the above three equations, the times of eight points around the minimum time T_0 can be obtained.

The above method is computationally expensive at $O(P^2)$ algebraic operations, where P denotes the total grid number. The computational times versus diverse grid numbers are shown in Fig. 3.

For I-SAFT imaging, the element spacing of the phase array is close to the wavelength, and the distance between the phase array and imaging area is at least quintuple the wavelength. The ultrasound meets the far-field approximation criteria, and the elements of the phase array can be treated as point sources [34]. The travel time from the point sources to each imaging position is theoretically computable

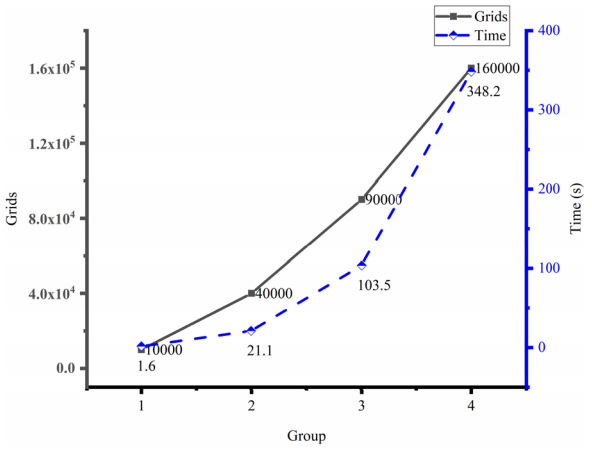

FIGURE 3. Computational times versus diverse grids numbers.

using this method, with the pre-knowledge of the acoustic parameters (shape and velocity) of cranial bones. Because the angles between the phase array and cranial bones are small in most circumstances, ultrasound mainly transforms to longitudinal waves in the cranial bones. The velocity of the cranial bones is therefore set as the longitudinal velocity for phase correction calculation in this paper. The corrected phases (travel time) are then used for I-SAFT reconstruction to improve the imaging quality.

III. SIMULATION AND EXPERIMENT

A. 3D PRINTED PHANTOM PREPATRATION

Cranial bones, including the occipital bone, two temporal bones, two parietal bones, the sphenoid, ethmoid and frontal bones, perform the leading role to form a cavity for the brain. The porosity of the squamous part of temporal bone is low and estimated to be close to that of cortical bone (retrieved from CT images originating from public resource of Magnetic Resonance Research Facility of University of Iowa Health Care). In the present paper, a sectional-piece image of the squamous part of the temporal bone was obtained from the public CT image resource. Ray-theory-based phase correction was implemented on the image. Fourteen cylindrical phantom bars (soft tissues) with different diameters (4.5 mm, 9.0 mm, 12.5 mm and 15.0 mm) were secured separately in the intracranial region. In addition, the other regions were filled with water. Photopolymer was selected as the tissue-mimicking material of the cranial bones. Its basic acoustic parameters, *i.e.*, longitudinal and shear velocity and attenuation, were respectively measured as $c_l = 2462$m/s, $c_s = 1129$m/s and $\alpha = 4$dB/MHz/cm by using the ultrasound transmission method [35]. The longitudinal velocity of the material was close to that of the cranial bones, and the material was thus suitable for phantom construction of cranial bones [36]. The X-ray CT image of the cranial bones was extended in the vertical direction and printed using a photopolymer 3D printer to prepare the cranial bone phantom. The cylindrical phantom bars were prepared using a mixture of carbon powder, agar, and water (weight ratio 1:3:96),

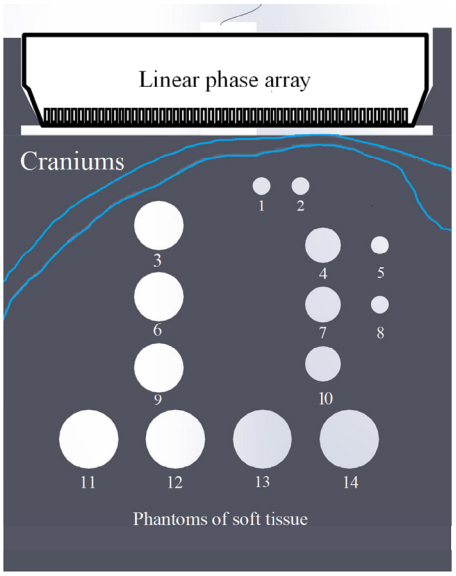

FIGURE 4. A schematic of the distribution of phase array probe, cranial bones phantom (surround by blue lines) and soft tissue phantoms.

whose shape in the final image can be used to evaluate the results after phase correction.

Both the simulation and experiment were performed with the same basic setting as shown in Fig. 4.

B. SIMUATION

The material parameters of the cranial bone phantom in the simulation were consistent with those of the photopolymer. The material parameters of soft tissues were uniformly and randomly distributed in space. The velocity distribution was $c = 1505 \pm 75\ m/\text{s}$, and the density distribution was $\rho = 1000 \pm 5kg/\text{m}^3$. Moreover, the velocity of water was $c = 1480\text{m/s}$ under the normal temperature (20°), and the density was $\rho = 1000\text{kg/m}^3$. The transmission signal was a Gaussian envelope pulse containing two sinusoidal cycles with a 1 MHz centre frequency. The full-wave simulations were implemented with the pseudospectrum time domain (PSTD) method [37]. The PSTD method assumes that all meshes have square shapes with the same sizes in the computational region. The mesh size was assigned as $dx = 0.11\ mm$, approximately one-thirteenth the wavelength $\lambda = 1.48\ mm$ in water and one-third the element spacing of the phase array. The time step was arranged to satisfy the Courant–Friedrich–Levy condition as 0.1 [37]. Two simulations were implemented altogether. The first one assumed the cranial bones to be liquid, where the shear wave in the bone was neglected in the simulation. The second one assumed the cranial bones as solid, where the longitudinal wave, shear wave and attenuation were all considered. The attenuation in water and soft tissues was ignored in the simulations.

C. EXPERIMENT

A linear array was secured outside the cranial phantom. The experiments were implemented with a customized phase array probe (128-element, 0.675 mm element spacing with −6 dB bandwidth from 0.5 MHz to 1.5 MHz) driven by a programmable ultrasound system (Vantage 128, Verasonics Inc, Kirkland, WA). The relative positions of the phantoms and phase array were fixed with additional 3D-printed assembly support. They were immersed in distilled water to finish the experiments under normal temperature (20°). The transmission signal in the experiment was the same as that of the simulation, and ten frames of signal acquisition were restored in total for offline reconstruction.

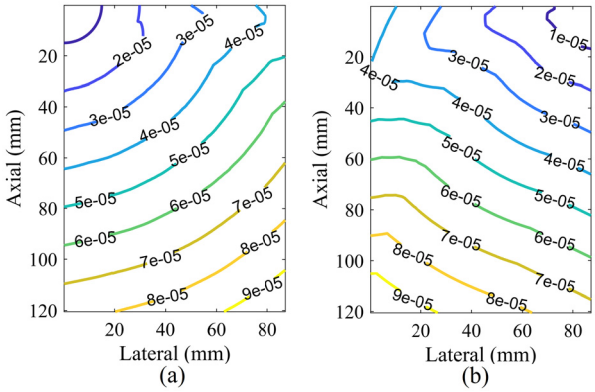

FIGURE 5. Contour lines with ultrasound emitted from (a) the first element, (b) the last element. The unit of the contour is milliseconds.

IV. RESULTS

A. SIMUATION

The phase-contour images are shown in Fig. 5, with ultrasound emitted from the first and last element of the phase array. The contour lines sweep across the whole imaging area, ensuring phase correction at each imaging position.

The reconstructed images with simulated signals are shown in Fig. 6. The shapes and positions of the cranial bones and soft tissues are exhibited in Fig. 6(a) without phase correction when the received signals are obtained from the first simulation. The corresponding image is exhibited in Fig. 6(b) after phase correction. The shapes and positions of the cranial bones and soft tissues are exhibited in Fig. 6(c) without phase correction when the received signals are obtained from the second simulation. The corresponding images are exhibited in Fig. 6(d) after phase correction. The reconstructed images are derived after a Wiener filtering process.

B. EXPERIMENT

Ten frames of experimental signals are averaged to reduce noise, and the reconstructed results are shown in Fig. 7. The images in the first row (see Fig. 7(a) and 7(b)) are the reconstructed results without phase correction, where soft tissues are distorted into quasi-ellipses. The images in the second row (see Fig. 7(c) and 7(d)) are obtained after phase correction, where distortions of soft tissues are intuitively corrected. The results (see Fig. 7(a) and 7(c)) are obtained using the DAS algorithm, and actual soft tissues are highlighted with dotted

TABLE 1. Errors of mean and standard deviation (SD) for uncorrected imaging and phase correction imaging (visible circle). ΔL denotes the center position shift, e represents the eccentricity of fitted ellipse. They are united to provide a standard for judging image distortion. In addition, C denotes the maximum luminance contrast to evaluated the extent of image enhancement. Median and interquartile range are displayed in the last column.

Number (Center L/mm , diameter R/mm)		Uncorrected imaging			Phase corrected imaging		
		$\Delta L/mm$ (mean±SD)	e (mean±SD)	C/dB (mean±SD)	$\Delta L/mm$ (mean±SD)	e (mean±SD)	C/dB (mean±SD)
[4]	[(69,34.1),9]	1.42±0.21	0.63±0.05	37.15±0.55	0.12±0.01	0.14±0.01	43.12±0.55
[5]	((83,34.5),4.5)	2.20±0.15	0.57±0.08	39.28±0.84	0.21±0.01	0.19±0.01	39.36±0.23
[6]	((26.5,47),12.5)	2.70±0.27	0.20±0.02	22.07±0.69	0.12±0.01	0.27±0.01	32.12±0.41
[7]	((69,49),9)	1.52±0.14	0.74±0.04	39.09±0.25	0.29±0.02	0.19±0.03	45.29±0.21
[8]	((83,49.5),4.5)	2.10±0.20	0.69±0.07	37.06±0.41	0.11±0.02	0.23±0.04	40.52±0.14
[9]	((26.5,66),12.5)	3.20±0.18	0.56±0.06	30.98±0.63	0.09±0.03	0.14±0.02	34.07±0.32
[10]	((69,64),9)	1.45±0.31	0.79±0.04	39.93±0.72	0.28±0.01	0.19±0.01	43.82±0.72
[12]	((31,83),15)	2.80±0.26	0.64±0.08	35.14±0.83	0.41±0.01	0.14±0.01	39.90±0.41
[13]	((53,83),15)	1.32±0.14	0.75±0.03	54.11±0.49	0.38±0.03	0.19±0.03	58.76±0.16
[14]	((73,83),15)	1.11±0.08	0.70±0.05	38.86±0.05	0.14±0.02	0.14±0.01	47.12±0.75
Total		1.98±0.20	0.63±0.06	37.36±0.60	0.21±0.02	0.19±0.02	42.41±0.52
Median, Interquartile Range (IQR)		2.06, 0.32	0.61, 0.11	38.24, 0.92	0.22, 0.03	0.19, 0.02	43.25, 0.95

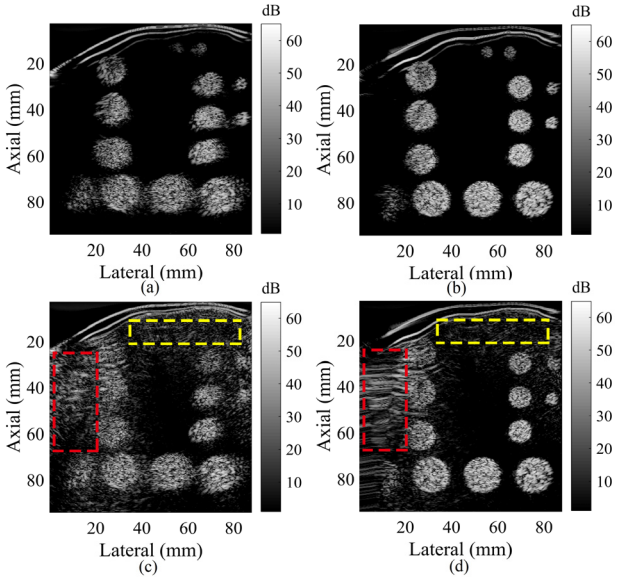

FIGURE 6. Simulated I-SAFT images with (a) conventional DAS with first simulation, (b) and DAS after phase correction; (c) conventional DAS with second simulation, (d) and DAS after phase correction. Obvious artifacts are marked by dotted lines.

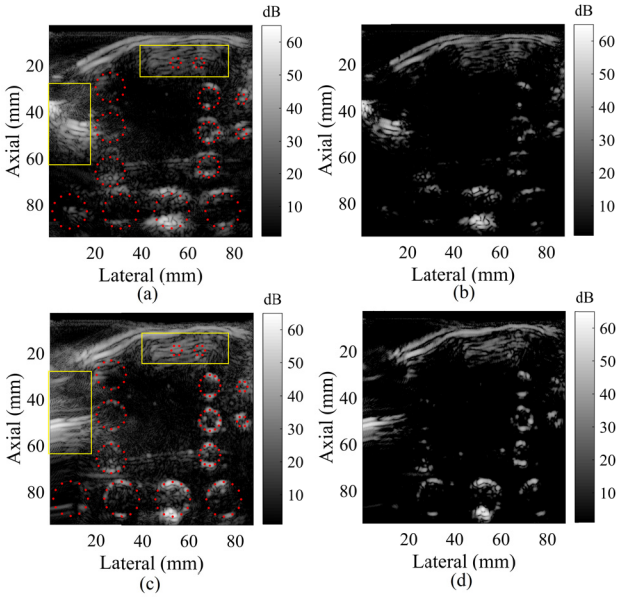

FIGURE 7. Experimental I-SAFT images with (a) conventional DAS (b) conventional DAS (wiener filtered), (c) DAS after phase correction (d) DAS after phase correction (wiener filtered).

circles. The images in Fig. 7(b) and 7(d) depict the corresponding Wiener-filtered results. Imaging noise is weakened, and the main structure of the soft tissues is more obvious after Wiener filtering. Experimental and simulation results are combined to evaluate the extent of distortion correction for transcranial imaging. The centre position shift, the eccentricity of the fitted ellipse and the maximum luminance contrast (difference between the maximum and minimum luminance values) for visible soft tissues (not degraded by artifact) are calculated and exhibited in Table 1.

V. DISCUSSION

The cranium-induced phase errors result in an offset in the spatial position, mainly manifested as a centre shift in this article; shape distortion, mainly manifested as a change from circular to quasi-elliptical in this article (see Figs. 6(a), 6(c), 7(a) and 7(b)). Such a phenomenon is expected to become obvious as applied for clinical usage because real tissues are continuous and because shape distortion causes aliasing. This aliasing degrades the distinction of different parts of intracranial tissues and thereby affects the accuracy of the diagnosis of brain disease. With the ray-theory-based phase correction, the images become accurate to reflect the spatial information of soft tissues, as shown in Figs. 6(b), 6(d), 7(c) and 7(d).

If only the longitudinal wave is taken into account for the PSTD simulation, the imaging quality improves. The

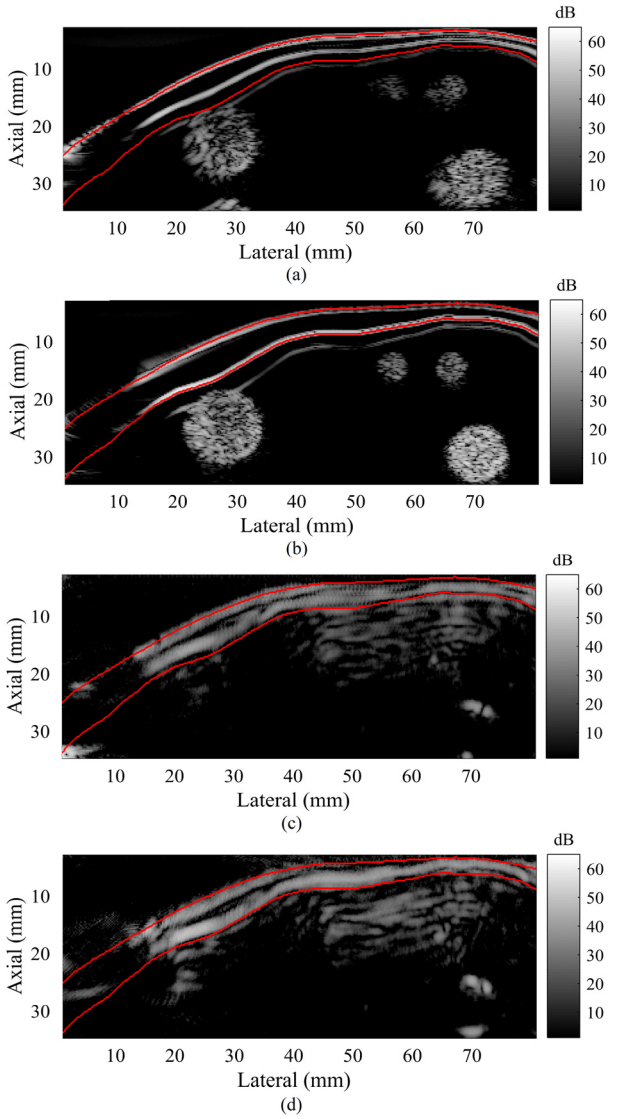

FIGURE 8. Images of cranial bone with I-SAFT using (a) conventional DAS and signals from the first simulation, (b) and corresponding DAS after phase correction; (c) conventional DAS and experimental signals (d) and corresponding DAS after phase correction. The true structure of bone is highlighted with lines.

shape, size, and spatial position of the cranial bones and soft tissues are consistent with the actual situation after phase correction, as displayed in Figs. 8(b) and 6(b). However, if the longitudinal wave and shear wave are taken into account for PSTD simulation, the imaging quality improves with some artifact. The soft tissues (No. 1 and No. 2) close to the lower surface of the cranial bones are obscured by artifact (marked by yellow dotted lines), and unexpected artifact (marked by red dotted lines) appear in the left potion of the image (see Fig. 6(c) and 6(d)). These artifact are caused by the longitudinal-shear-longitudinal mode conversion, which cannot readily be eliminated because only longitudinal waves are reserved for ray-theory-based phase correction.

Limited by the low centre frequency, wide spacing width of phased array and unexpected noise, the resolution of I-SAFT images is low in our experiments [38]. Only the upper and lower parts of the soft tissues are visible, and internal details are poorly imaged. Such a phenomenon also appears in structure imaging of cranial bones (see Fig. 8(b) and 8(d)). The shape, size and spatial position of soft tissues, as well as the artifact (marked by yellow solid lines) in experimental results (see Fig. 7(a) and 7(c)), are approximately similar to those of the second simulation (see Fig. 6(c) and 6(d)). The centre position shift and eccentricity of the fitted ellipse of the soft tissues are chosen as two standards to evaluate the extent of phase correction. The two standards of ten visible soft tissues are compared between reconstructed images and actual situations (dotted line). With conventional reconstruction, the centre position shifts of the soft tissues (No. 6, No. 9 and No. 12) on the left portion are overall larger than those of the other tissues (see Figs. 4 and 7). This is because the left part of the present cranial bone phantom is thicker than the right part. In addition, the eccentricity of the quasi-ellipse in the right part (No. 7, No. 8, No. 10 and No. 13) is larger than that in the left part (see Figs. 4 and 7). This is because the irregularity of the present cranial bone phantom on the right is relatively high, causing more significant refraction than its counterpart in the left. The statistical information indicates that the centre position shift has increased from 1.98 ± 0.20 mm to 0.21 ± 0.02 mm (mean $\pm$ SD), and the eccentricity of the quasi-ellipse has increased from 0.63 ± 0.06 to 0.19 ± 0.02 (mean $\pm$ SD), after ray-theory-based phase correction. In addition, the contrast value of those soft tissues has evidently improved according to the simulation and experimental results (see Figs. 6 and 7). The statistical information from the experimental results indicates that the average maximum luminance contrast has improved from 37.36 ± 0.60 dB to 42.41 ± 0.52 dB (mean $\pm$ SD) after ray-theory-based phase correction.

The ray-theory-based phase correction method has a wider imaging area than the limited beacon points with the time-reversal method. It is also more universal and accurate than the auto-correlation method, in which the thickness compensation of cranial bones is necessary for accurate imaging [13]. The ray-theory-based phase correction has higher efficiency than full-wave simulation-based phase correction, while acoustic parameters are essential for those two methods. There are also some limitations of the present method. For example, mode-conversion-induced artifact cannot readily be eliminated; the phase correction relies on the pre-knowledge of cranial bones; the method cannot accurately correct the phases with anisotropic cranial bones, etc.

VI. CONCLUSION

Transcranial imaging correction is achieved by combining the ray-theory-based phase correction method and synthetic focusing aperture technology. With the pre-knowledge of the spatial position and longitudinal wave speed of the cranial bones, dynamic focusing is achieved at each imaging position. Simulation and experiment indicate that the proposed method can be used to improve the accuracy and contrast

of transcranial imaging. The quantitative results demonstrate that the presented method can decrease the average error of the central position of the soft tissues from 1.98 mm to 0.21 mm and the average eccentricity of the fitted ellipse of the soft tissues from 0.63 to 0.19. The average maximum luminance contrast improves from 37.36 dB to 42.41 dB with ray-theory-based phase correction. Future investigations will be focused on a method for realizing phase correction imaging without knowing the bone morphology. Machine learning (ML) has the potential to revolutionize brain disease diagnosis by performing classification and efficient management by rapidly reviewing medical images. Higher-quality brain images are required to guarantee the reliability of both training data and test data, which helps to improve the accuracy of brain disease classification.

REFERENCES

[1] C. Marant-Micallef, K. D. Shield, J. Vignat, E. Cléro, A. Kesminiene, C. Hill, A. Rogel, B. Vacquier, F. Bray, D. Laurier, and I. Soerjomataram, "The risk of cancer attributable to diagnostic medical radiation: Estimation for France in 2015," *Int. J. Cancer*, vol. 144, pp. 2954–2963, Jun. 2018.

[2] M. R. Mann *et al.*, "Breast MRI: EUSOBI recommendations for women's information," *Eur. Radiol.*, vol. 25, no. 12, pp. 3669–3678, Dec. 2015.

[3] M. Groth, M. Ernst, P. Deindl, and J. Herrmann, "B-flow sonography for evaluation of basal cerebral arteries in newborns," *Clin. Neuroradiol.*, vol. 29, no. 1, pp. 95–100, Mar. 2019.

[4] D.-H. Li, Y.-C. He, J. Liu, and S.-D. Chen, "Diagnostic accuracy of transcranial sonography of the substantia nigra in Parkinson's disease: A systematic review and Meta-analysis," *Sci. Rep.*, vol. 6, no. 1, p. 20863, Feb. 2016.

[5] D. Berg, J. Godau, and U. Walter, "Transcranial sonography in movement disorders," *Lancet Neurol.*, vol. 7, no. 11, pp. 1044–1055, Nov. 2008.

[6] V. Chaplin, M. A. Phipps, and C. F. Caskey, "A random phased-array for MR-guided transcranial ultrasound neuromodulation in non-human primates," *Phys. Med. Biol.*, vol. 63, no. 10, May 2018, Art. no. 105016.

[7] V. Krishna, F. Sammartino, and A. Rezai, "A review of the current therapies, challenges, and future directions of transcranial focused ultrasound technologyadvances in diagnosis and treatment," *JAMA. Neurol.*, vol. 75, no. 2, pp. 246–254, Feb. 2018.

[8] L. Marsac, D. Chauvet, R. L. Greca, A.-L. Boch, K. Chaumoitre, M. Tanter, and J.-F. Aubry, "Ex vivo optimisation of a heterogeneous speed of sound model of the human skull for non-invasive transcranial focused ultrasound at 1MHz," *Int. J. Hyperthermia*, vol. 33, no. 6, pp. 635–645, Mar. 2017.

[9] C. P. A. Wapenaar and J. L. T. Grimbergen, "Reciprocity theorems for one-way wavefields," *Geophys. J. Int.*, vol. 127, no. 1, pp. 169–177, Oct. 1996.

[10] M. Fink, G. Montaldo, and M. Tanter, "Time reversal acoustics," in *Proc. IEEE Ultrason. Symp.*, Aug. 2004, pp. 850–859. [Online]. Available: https://ieeexplore.ieee.org/abstract/document/1417870

[11] M. Tanter, J.-F. Aubry, J. Gerber, J. L. Thomas, and M. Fink, "Optimal focusing by spatio-temporal inverse filter. I. Basic principles," *J. Acoust. Soc. Amer.*, vol. 110, no. 1, pp. 37–47, Aug. 2001.

[12] J. F. Aubry, M. Tanter, J. Gerber, J.-L. Thomas, and M. Fink, "Optimal focusing by spatio-temporal inverse filter. II. Experiments. application to focusing through absorbing and reverberating media," *J. Acoust. Soc. Amer.*, vol. 110, no. 1, pp. 48–58, Aug. 2001.

[13] D. E. Soulioti, D. Espíndola, P. A. Dayton, and G. Pinton, "Super resolution imaging through the human skull," 2018, *arXiv:1811.10653*. [Online]. Available: https://arxiv.org/abs/1811.10653

[14] F. Vignon, J.-F. Aubry, M. Tanter, A. Margoum, and M. Fink, "Adaptive focusing for transcranial ultrasound imaging using dual arrays," *J. Acoust. Soc. Amer.*, vol. 120, no. 5, pp. 2737–2745, Aug. 2015.

[15] N. M. Ivancevich, G. F. Pinton, H. A. Nicoletto, E. Bennett, D. T. Laskowitz, and S. W. Smith, "Real-time 3-D contrast-enhanced transcranial ultrasound and aberration correction," *Ultrasound Med. Biol.*, vol. 34, no. 9, pp. 1387–1395, Sep. 2008.

[16] M. Hajian, R. Gaspar, and R. G. Maev, "Accurate 3-D profile extraction of skull bone using an ultrasound matrix array," *IEEE Trans. Biomed. Eng.*, vol. 64, no. 12, pp. 2858–2871, Dec. 2017.

[17] B. D. Lindsey and S. W. Smith, "Pitch-catch phase aberration correction of multiple isoplanatic patches for 3-D transcranial ultrasound imaging," *IEEE Trans. Ultrason., Ferroelectr., Freq. Control*, vol. 60, no. 3, pp. 463–480, Mar. 2013.

[18] G. Clement, P. White, and K. Hynynen, "Enhanced ultrasound transmission through the human skull using shear mode conversion," *J. Acoust. Soc. Amer.*, vol. 115, no. 3, pp. 1356–1364, Mar. 2004.

[19] S. Almquist, D. L. Parker, and D. A. Christensen, "Rapid full-wave phase aberration correction method for transcranial high-intensity focused ultrasound therapies," *J. Therapeutic Ultrasound*, vol. 4, no. 1, pp. 30–41, Dec. 2004.

[20] F. Marquet, A. L. Boch, M. Pernot, G. Montaldo, D. Seilhean, M. Fink, M. Tanter, and J.-F. Aubry, "Non-invasive ultrasonic surgery of the brain in non-human primates," *J. Acoust. Soc. Amer.*, vol. 134, no. 2, pp. 1632–1639, Aug. 2013.

[21] N. Jiménez, F. Camarena, J. Redondo, V. Sánchez-Morcillo, Y. Hou, and E. E. Konofagou, "Time-domain simulation of ultrasound propagation in a tissue-like medium based on the resolution of the nonlinear acoustic constitutive relations," *Acta Acustica United With Acustica*, vol. 102, no. 5, pp. 876–892, Sep. 2016.

[22] X. Jin, C. Li, and L. V. Wang, "Effects of acoustic heterogeneities on transcranial brain imaging with microwave-induced thermoacoustic tomography," *Med. Phys.*, vol. 35, no. 7, pp. 3205–3214, Jun. 2008.

[23] R. M. Jones, M. A. O'Reilly, and K. Hynynen, "Transcranial passive acoustic mapping with hemispherical sparse arrays using CT-based skull-specific aberration corrections: A simulation study," *Phys. Med. Biol.*, vol. 58, no. 14, pp. 4981–5005, Jun. 2013.

[24] N. Rawlinson, J. Hauser, and M. Sambridge, "Seismic ray tracing and wavefront tracking in laterally heterogeneous media," *Adv. Geophys.*, vol. 49, pp. 203–273, May 2008.

[25] B. van Ginneken, M. Stavridi, and J. J. Koenderink, "Diffuse and specular reflectance from rough surfaces," *Appl. Opt.*, vol. 37, no. 1, pp. 130–139, Jan. 1998.

[26] S. Jeon, J. Park, R. Managuli, and C. Kim, "A novel 2-D synthetic aperture focusing technique for acoustic-resolution photoacoustic microscopy," *IEEE Trans. Med. Imag.*, vol. 38, no. 1, pp. 250–260, Jul. 2018.

[27] C.-I. C. Nilsen and S. Holm, "Wiener beamforming and the coherence factor in ultrasound imaging," *IEEE Trans. Ultrason., Ferroelectr., Freq. Control*, vol. 57, no. 6, pp. 1329–1346, Jun. 2010.

[28] C. Errico, J. Pierre, S. Pezet, Y. Desailly, Z. Lenkei, O. Couture, and M. Tanter, "Ultrafast ultrasound localization microscopy for deep super-resolution vascular imaging," *Nature*, vol. 527, no. 7579, pp. 499–502, Nov. 2015.

[29] M. Toulemonde, Y. Li, S. Lin, F. Cordonnier, and M. Butler, "High-frame-rate contrast echocardiography using diverging waves: Initial *in vitro* and *in vivo* evaluation," *IEEE Trans. Ultrason., Ferroelectr., Freq. Control*, vol. 65, no. 12, pp. 2212–2221, Dec. 2018.

[30] Y. Lu, H.-Y. Tang, S. Fung, B. E. Boser, and D. A. Horsley, "Pulse-echo ultrasound imaging using an AlN piezoelectric micromachined ultrasonic transducer array with transmit beam-forming," *J. Microelectromech. Syst.*, vol. 25, no. 1, pp. 179–187, Feb. 2016.

[31] Y. Liu and M. K. Sen, "A new time-space domain high-order finite-difference method for the acoustic wave equation," *J. Comput. Phys.*, vol. 228, no. 23, pp. 8779–8806, Dec. 2009.

[32] P. G. Bergmann, Ed., "Ray acoustic," in *Physics of Sound in the Sea*. Washington DC, USA: National Defense Research Council Division, 1946, pp. 41–68. [Online]. Available: https://archive.org/stream/physicsofsoundin00rese#page/40/mode/2up

[33] F. H. Qin, Y. Luo, K. B. Olsen, W. Y. Cai, and G. T. Schuster, "Finite-difference solution of the eikonal equation along expanding wavefronts," *Geophysics*, vol. 57, no. 3, pp. 478–487, Mar. 1992.

[34] J. A. Jensen and N. B. Svendsen, "Calculation of pressure fields from arbitrarily shaped, apodized, and excited ultrasound transducers," *IEEE Trans. Ultrason., Ferroelectr., Freq. Control*, vol. 39, no. 2, pp. 262–267, Mar. 1992.

[35] L. Peralta, X. Cai, P. Laugier, and Q. Grimal, "A critical assessment of the *in-vitro* measurement of cortical bone stiffness with ultrasound," *Ultrasonics*, vol. 80, pp. 119–126, Sep. 2017.

[36] S. Pichardo, C. Moreno-Hernández, R. A. Drainville, V. Sin, L. Curiel, and K. Hynynen, "A viscoelastic model for the prediction of transcranial ultrasound propagation: Application for the estimation of shear acoustic properties in the human skull," *Phys. Med. Biol.*, vol. 62, no. 17, pp. 6938–6962, Aug. 2017.

[37] J. Xie, Z. Guo, H. Liu, and Q. H. Liu, "GPU acceleration of time gating based reverse time migration using the pseudospectral time-domain algorithm," *Comput. Geosci.*, vol. 117, pp. 57–62, Aug. 2018.
[38] J. T. Ylitalo and H. Ermert, "Ultrasound synthetic aperture imaging: Monostatic approach," *IEEE Trans. Ultrason., Ferroelectr., Freq. Control*, vol. 41, no. 3, pp. 333–339, May 1994.

CHEN JIANG was born in Shandong, China, in 1992. He received the B.S. degree from the Department of Marine Technology, Ocean University of China, Qingdao, China, in 2014, and the M.S. degree from the Department of Acoustic Science and Engineering, Nanjing University. He is currently pursuing the Ph.D. degree in biomedical engineering with the Department of Electronic Engineering, Fudan University, Shanghai, China. His main research interests include biomedical ultrasound, signal processing, and ultrasound nondestructive imaging.

YUNQING LI was born in Tianjin, China, in 1995. She received the B.S. degree from the Department of Electronic Engineering, Fudan University, Shanghai, China, in 2018, where she is currently pursuing the M.S. degree in biomedical engineering. Her research interests include biomedical ultrasound imaging and signal processing.

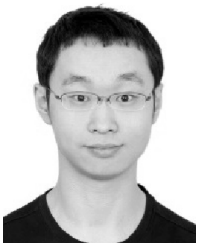

BOYI LI was born in Hohhot, China, in 1990. He received the B.S. degree from the Department of Information and Engineering Technology, Sichuan Agricultural University, Ya'an, China, in 2012, and the M.S. degree from the Department of Electronic and Information Engineering, Inner Mongolia University, Hohhot, in 2015. He is currently pursuing the Ph.D. degree in biomedical engineering with the Department of Electronic Engineering, Fudan University, Shanghai, China. His main research interests include biomedical ultrasound, signal processing, and statistical analysis.

CHENGCHENG LIU was born in Shandong, China, in 1987. He received the B.S. and Ph.D. degrees from the Department of Electronic Engineering, Fudan University, China, in 2009 and 2014, respectively. He was a Postdoctoral Researcher with the Department of Electronic Engineering, Fudan University, from 2014 to 2016. He is currently an Assistant Professor with the School of Physics Science and Engineering, Institute of Acoustics, Tongji University. His research interests include biomedical ultrasound, ultrasonic signal processing, and ultrasonic imaging.

FENG XU was born in Nanjing, China, in 1982. He received the B.S. degree from the Department of Electronic Information Science and Technology, Nanjing University of Posts and Telecommunications, in 2005, and the Ph.D. degree from the Department of Electronic Engineering, Fudan University, in 2010. He is currently a Senior Engineer with the Department of Electronic Engineering, Fudan University. His research interests include ultrasonic signal processing and system design.

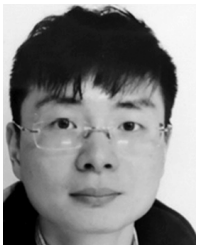

KAILIANG XU (M'14) received the Ph.D. degree in biomedical engineering from Fudan University, Shanghai, China, in 2012. He is currently an Associate Professor with the Department of Electronic Engineering, Fudan University. His research interests include wave simulation, signal processing, inverse problem, the development of multi-wave imaging techniques, and elasticity characterization for medical ultrasound and non-destructive evaluation.

DEAN TA was born in China in 1972. He received the M.S. degree from the Institute of Acoustics, Shaanxi Normal University, Xi'an, China, in 1999, and the Ph.D. degree from Tongji University, Shanghai, China, in 2002. From 2002 to 2004, he was a Postdoctoral Researcher with the Department of Electronic Engineering, Fudan University, Shanghai, where he is currently a Professor. He has contributed over 130 articles, has coauthored one book, and holds five patents. His research interests include biomedical ultrasound, medical signal processing, diagnosis systems of medical ultrasound, and applications of ultrasonic guided waves in medicine and nondestructive examination. He is currently the Vice-Chairman of the Biomed Ultrasound Speciality of the Chinese Society of Acoustics and a Standing Committee Member of the Apparatus Engineering Speciality of the Chinese Association of Ultrasound in Medicine and Engineering.